Spatial patterns of climate change across the Paleocene–Eocene Thermal Maximum

Jessica E. Tierney[a,1] , Jiang Zhu[b], Mingsong Li[c] , Andy Ridgwell[d] , Gregory J. Hakim[e] , Christopher J. Poulsen[f] , Ross D. M. Whiteford[g] , James W. B. Rae[g] , and Lee R. Kump[h]

The Paleocene–Eocene Thermal Maximum (PETM; 56 Ma) is one of our best geological analogs for understanding climate dynamics in a "greenhouse" world. However, proxy data representing the event are only available from select marine and terrestrial sedimentary sequences that are unevenly distributed across Earth's surface, limiting our view of the spatial patterns of climate change. Here, we use paleoclimate data assimilation (DA) to combine climate model and proxy information and create a spatially complete reconstruction of the PETM and the climate state that precedes it ("PETM-DA"). Our data-constrained results support strong polar amplification, which in the absence of an extensive cryosphere, is related to temperature feedbacks and loss of seasonal snow on land. The response of the hydrological cycle to PETM warming consists of a narrowing of the Intertropical Convergence Zone, off-equatorial drying, and an intensification of seasonal monsoons and winter storm tracks. Many of these features are also seen in simulations of future climate change under increasing anthropogenic emissions. Since the PETM-DA yields a spatially complete estimate of surface air temperature, it yields a rigorous estimate of global mean temperature change (5.6 °C; 5.4 °C to 5.9 °C, 95% CI) that can be used to calculate equilibrium climate sensitivity (ECS). We find that PETM ECS was 6.5 °C (5.7 °C to 7.4 °C, 95% CI), which is much higher than the present-day range. This supports the view that climate sensitivity increases substantially when greenhouse gas concentrations are high.

Paleocene–Eocene Thermal Maximum | greenhouse climates | climate sensitivity | hydrological cycle | data assimilation

The Paleocene–Eocene Thermal Maximum (PETM)—a global warming that occurred 56 Ma—is one of the best-studied "hyperthermal" events (1). Driven by a geologically rapid [ca. 3 to 10 ky (2)] release of mostly volcanic CO_2 (3, 4), previous estimates place the magnitude of global warming around 4 °C to 5 °C (5–7). In addition to warming, the ocean acidified (8) and underwent deoxygenation (9). Terrestrial and near-shore marine records document a substantial alteration in the hydrological cycle, with elevated precipitation in the high latitudes and an increase in extreme flood events (10–12). Given the geological rapidity of the event and the magnitude of climatic disruption, the PETM offers valuable lessons for how the climate system responds to sudden increases in greenhouse gases (13).

Through the efforts of ocean drilling and outcrop work, the PETM has been documented in all ocean basins and on all major land masses (1, 5, 12, 14). However, the locations where climate change is reliably resolved across the event are more limited and are unevenly distributed in space. This renders the determination of the magnitude of global warming challenging; existing inferences are dependent on the averaging method and have absolute uncertainties on the order of 8 °C to 10 °C (90% CI) and a relative uncertainty of 3.4 °C (90% CI) (7). Likewise, although research to date documents polar amplification and strong regional warming (5, 15), the spatial patterns of temperature and hydrological cycle changes across the PETM are difficult to derive from the sparse proxy network alone. Conversely, climate model simulations using Eocene boundary conditions and elevated atmospheric CO_2 concentrations can provide guidance on what the patterns of climate change might have looked like, but they exhibit large intermodel spread and may not match proxy information (5, 6, 12, 16).

In order to better estimate the magnitude and spatial patterns of climatic changes during the PETM, we combine information from proxy indicators of temperature with isotope-enabled model simulations using data assimilation (DA). The DA technique blends proxy and model data in a formal statistical framework and offers a number of advantages over traditional proxy–model comparison. For one, in DA, the comparison between proxies and models (the "innovation" step) can take place in native proxy units, which is advantageous for proxies that are influenced by more than one climatic

Significance

The Paleocene–Eocene Thermal Maximum (PETM) is a global warming event that occurred 56 Ma in response to an increase in carbon dioxide. Geological data from the PETM are only available from a few places, which makes it difficult to get a global view of what happened. Here, we use a technique called data assimilation to create maps of PETM climate. We find that changes in temperature and rainfall during the PETM are similar to future projections of climate change. We also calculate "climate sensitivity"—how much the Earth warms when carbon dioxide levels are doubled. We find that PETM sensitivity is much higher than today, which suggests the Earth becomes more sensitive to greenhouse gas emissions as they increase.

parameter (e.g., the oxygen isotopic composition of foraminifera). Second, DA spreads proxy information spatially by using the covariance structure of the climate model. Hence, a proxy influences the posterior result not only at the location where it exists but also, in regions whose variability is closely connected to the proxy location. Third, DA allows for proxy information to update multiple climate fields at once, including climatically relevant quantities for which we have no direct indicators for (e.g., cloud cover) but are related to what the proxies record (e.g., sea surface temperature; SST). Finally, in the case of an ancient climate event, like the PETM, where atmospheric carbon dioxide concentrations and climate sensitivity are poorly constrained, the DA approach allows us to statistically "select" model simulations that match the proxy information best from a large potential pool of equally possible climate states (e.g., three vs. six vs. nine times preindustrial CO_2; different orbital configurations).

We incorporate four types of paleotemperature data into the DA: the oxygen isotopic composition ($\delta^{18}O$) of well-preserved ("glassy") planktic foraminifera, the magnesium-to-calcium ratio (Mg/Ca) of planktic foraminifera, TEX_{86} (the tetraether index of 86 carbons based on marine isoprenoidal glycerol dialkyl glycerol tetraethers [GDGTs]), and $MBT^{5'}_{Me}$ (the methyl branched tetraether index based on terrestrial branched GDGTs) (Fig. 1). Each of these temperature proxy types has an established forward model that relates the proxy units to environmental influences in a physically and statistically robust way, facilitating their use in the DA framework (*SI Appendix*). For the model simulations, we use a set of Early Eocene experiments run with the isotope-enabled Community Earth System Model 1.2 (iCESM 1.2) (19, 20). These simulations followed the boundary conditions from the Deep-Time Model Intercomparison Project (deepMIP) (18) and were run across different CO_2 concentrations (3 to 11 times preindustrial atmospheric concentrations) and orbital configurations (*SI Appendix*). The model and proxy data were combined using the offline DA method described in refs. 21 and 22 (*SI Appendix*) to produce an estimate of the pre-PETM and PETM climate state, respectively.

The resulting product, the "PETM-DA," is spatially complete, allowing us to obtain an improved estimate of global temperature change, as well as climate sensitivity, during this extreme warm climate state. In the offline DA method used here, the spatial patterns of the PETM-DA are based on the covariance structures in the model; effectively, the PETM-DA represents the model-derived patterns of climate change that best match the proxy information. However, the model prior is broad, allowing for many different possible patterns of change. Moreover, because the PETM-DA inherits the physical constraints of the climate model, we can leverage the multiple physically consistent fields in the posterior ensemble to investigate the drivers of the spatial changes in temperature and hydroclimate during the event.

Results and Discussion

Temperature Change. The PETM-DA indicates that global mean surface temperature (GMST) during the PETM and just prior to the event (the "pre-PETM") was 34.1 °C (33.1 °C to 35.5 °C, 95% CI) and 28.5 °C (27.5 °C to 30.1 °C, 95% CI), respectively, which reflect a substantial narrowing (i.e., "learning" from the proxy data) over the broad model prior (24.6 °C to 41.7 °C) (Fig. 2B). This indicates a global warming of 5.6 °C (5.4 °C to 5.9 °C, 95% CI) (Fig. 2B), which is similar to but slightly higher than previous proxy only–based estimates of 5 °C to 5.3 °C (6, 7, 15). However, with the exception of ref. 15, previous work generally did not consider the "pH effect" on the $\delta^{18}O$ of planktic foraminifera. pH has a large impact on the $\delta^{18}O$ paleothermometer because it controls the speciation of dissolved CO_2 in seawater, which imparts a change in isotopic fractionation (23–25). When ocean pH is low, such as during the PETM [ca. 7.4, potentially lasting for tens of thousands of years (3)], the $\delta^{18}O$ of carbonate is higher, leading to systematic underestimation of warmth if pH changes are not accounted for (26). The pH effect is built into our forward modeling following the method of ref. 25 (*SI Appendix*). Sensitivity testing shows that inclusion of the pH effect in forward modeling increases the estimated change in GMST during the PETM by 0.9 °C (from a median of 4.7 °C to 5.6 °C) (*SI Appendix*, Fig. S1).

The spatial expression of warming during the PETM reveals that land areas warmed more than the ocean and that there was substantial polar amplification (Fig. 2 A and C). Relative to the prior mean, the pre-PETM and PETM posterior means show that different spatial patterns emerge with the addition of the proxy data in each time interval, with the PETM posterior emphasizing warmth over the northern high latitudes (*SI Appendix*, Fig. S2F). On average, the polar regions (60 °N to 90 °N and 60 °S to 90 °S) warmed by 8 °C, whereas the low latitudes (30 °S to 30 °N) warmed by 5 °C, yielding a 3 °C decrease in the meridional temperature gradient (*SI Appendix*, Fig. S2D). High-latitude warming is especially pronounced over the Antarctic continent, where it approaches 12 °C in the interior (Fig. 2C). In icehouse climates, like present day or the moderately warmer Pliocene, surface–albedo feedbacks associated with declining land or sea ice cover are the largest driver of polar amplification (27, 28). However, there is no prescribed land ice and only minimal seasonal sea ice in the model that prior simulations used for the PETM-DA. We do, however, find that the pre-PETM posterior state has nonnegligible amounts of seasonal snow cover that build up in the austral winter over most of the Antarctic interior. This snow cover persists into austral spring and has a substantial radiative impact through increased albedo (*SI Appendix*, Fig. S3). During the PETM, Antarctic snow cover is thinner (*SI Appendix*, Fig. S3D) and lasts a shorter period, lowering surface albedo and contributing to magnified warming over Antarctica (Fig. 2 A and C). There are no proxies available from inland Antarctica to assess whether seasonal Antarctic snow is reasonable. Clay mineral assemblages from Site Ocean Drilling
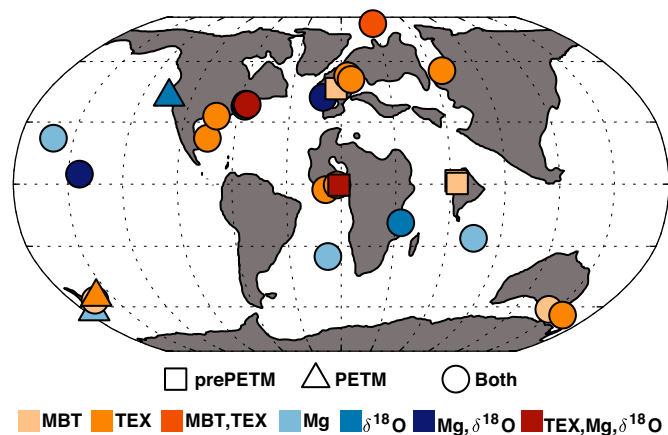
Fig. 1. Location and types of temperature proxies that inform the PETM-DA. Data are plotted on the plate reconstruction of ref. 17, which is used in the deepMIP project boundary conditions (18) and for the climate simulations in this study. Squares indicate locations with pre-PETM data only, triangles indicate locations with PETM data only, and circles indicate locations with data for both the pre-PETM and PETM. $\delta^{18}O$, $\delta^{18}O$ of planktic foraminifera; MBT, $MBT^{5'}_{Me}$; Mg, Mg/Ca of planktic foraminifera; TEX, TEX_{86}.

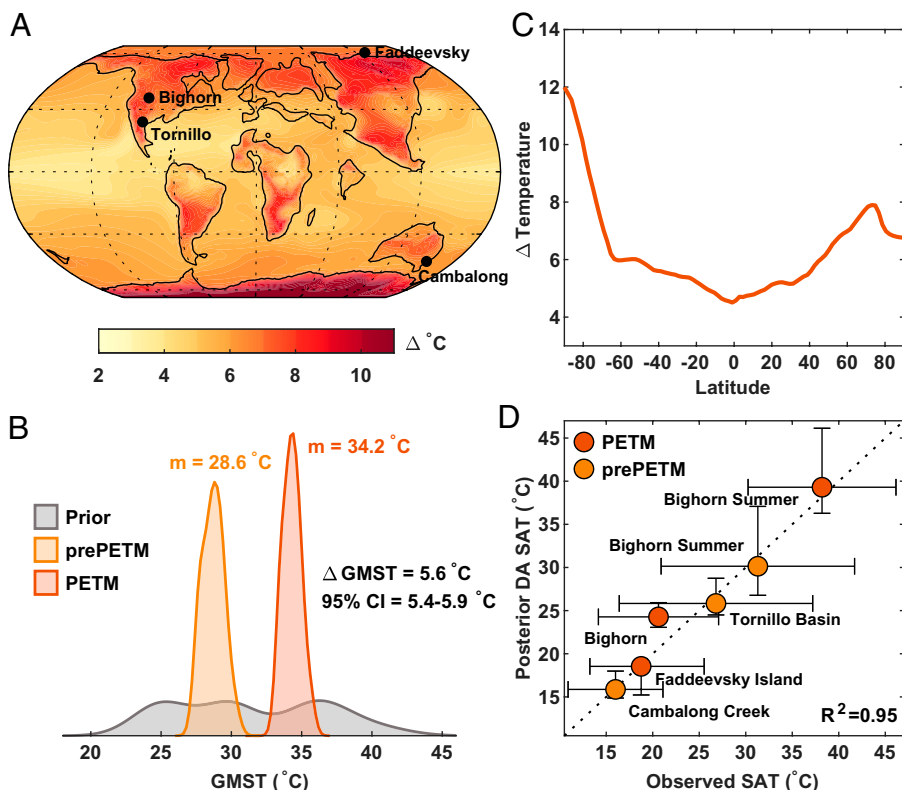**Fig. 2.** Temperature changes during the PETM event. (*A*) Mean annual surface air temperature anomalies during the PETM, relative to the pre-PETM state, overlain with the locations of the terrestrial temperature proxy data plotted in *D*. (*B*) Kernel density estimates of GMST in the model prior simulations (gray) and in the posterior DA solutions for the pre-PETM (orange) and PETM (red). Median ΔGMST for the PETM − pre-PETM and the 95% CI are also shown. (*C*) Zonal mean annual surface air temperature change. (*D*) Validation of PETM-DA surface air temperature (SAT) against independent terrestrial temperature proxies; error bars represent 95% CIs (Dataset S2 and *SI Appendix*).

Program (ODP) 690 suggest coastal Antarctic temperatures must have been at least 15 °C (29); the PETM-DA results agree with these data, indicating that temperatures at the coastal grid cell closest to Site 690 remained above 13 °C year round. A warm coast, however, does not preclude seasonal snow cover in the interior, especially if central Antarctic elevations were 1,000 to 2,000 m (30).

In the Arctic region, peak warming occurred over land, with the ocean showing less amplification (Fig. 2 *A* and *C*). There is some loss of spring snow in the interior regions of the Arctic landmasses during the PETM that contributes to elevated warming (*SI Appendix*, Fig. S3B); however, the oceanic amplification is more likely related to atmospheric changes. Temperature feedbacks, including lapse rate and Planck, as well as poleward atmospheric latent heat transport are known atmospheric processes that contribute to polar amplification independently of snow and ice changes (28). In addition, while the PETM-DA shows that the biggest changes in low cloud cover occur over the subtropical (upwelling zone) regions, clouds also decreased by 10 to 15% over the Southern Ocean and the Northern Hemisphere midlatitudes (*SI Appendix*, Fig. S4), and likely contributed to the elevated warming (Fig. 2*C*). A strong shortwave cloud feedback is a feature of the Community Earth System Model (CESM) simulations that was previously shown to contribute to mid- to high-latitude warming, as both cloud cover and opacity decline nonlinearly with increasing CO_2 (6).

As an independent validation exercise, we compared the PETM-DA results with pollen, leaf-based, and clumped isotope terrestrial temperature proxies that were not assimilated. Although these independent proxy data are limited in number and spatial representation, we find that the PETM-DA overlaps with

these estimates within uncertainties, with a good one-to-one correspondence (Fig. 2*D*). The PETM-DA produces summer temperatures at the Bighorn basin site that are in excellent agreement with those derived from clumped isotope analyses of soil carbonates (31) and also, reproduces warmth in the high Arctic [Faddeevsky Island, paleolatitude of ca. 80 °N (32)]. Notably, the PETM-DA posterior shows a better match to these independent proxies ($R^2 = 0.95$) than the model prior mean ($R^2 = 0.70$), which predicts the pre-PETM temperatures well but underestimates PETM temperatures (*SI Appendix*, Fig. S5). This indicates that the assimilation of the SST proxies produces a posterior state that is in better agreement with the terrestrial proxies than the model on its own. Crucially, the PETM-DA remains above freezing during the winter months in the Arctic Ocean and midlatitude North America, in agreement with paleobotanical evidence (31–33) (*SI Appendix*, Fig. S6). Freezing temperatures during the PETM are limited to the continental interior of northeast Asia and northwesternmost North America and to the Antarctic interior (*SI Appendix*, Fig. S6). Taken together, these comparisons give us confidence that the PETM-DA is yielding a plausible solution for the magnitude and general pattern of warmth during the PETM.

Hydroclimate Change. The DA method allows for the inclusion of any number of climate variables in the model prior state vector, all of which get updated with the proxy information through the covariance calculation in the Kalman filter (*SI Appendix*, Eqs. 1 and 2). Thus, although we did not assimilate hydroclimate proxies, we can still obtain posterior solutions for hydroclimatic variables, including precipitation (P), evaporation (E), and the hydrogen isotopes of precipitation (δD_P). These fields reflect what

the temperature proxy data imply about hydroclimatic change during the PETM based on the covariance between temperature and hydroclimate inherent to the model's physics.

The DA result indicates that $P - E$ increased during the PETM near the equator and in the high latitudes and decreased in off-equatorial and some subtropical regions, in broad agreement with independent proxy evidence (Fig. 3A). In the equatorial and high-latitude regions, the observed changes are mainly due to higher rates of precipitation (*SI Appendix*, Fig. S7). In the Pacific and Atlantic basins, off-equatorial drying is primarily driven by decreased precipitation, while evaporation contributes more to reduced $P - E$ in the Tethys Ocean (*SI Appendix*, Fig. S7). The subtropics show a muted response in the zonal mean (Fig. 3B), reflecting regional heterogeneity.

The zonal mean hydrological response between 20 °S and 20 °N indicates a narrowing of the ITCZ (Fig. 3B), a phenomenon also observed in the instrumental record (35, 36) and climate model experiments run under future greenhouse gas emissions scenarios (36–38). The tendency for the ITCZ to narrow in a warmer climate is related to an increase in the meridional moist static energy gradient, which exports energy from the tropics and thus, requires an increase in upward mass flux in the ITCZ (38). As ITCZ rainfall intensifies, the off-equatorial regions at the margins of convection dry out, consistent with the "upped-ante" mechanism (39). Although changes in ITCZ width and strength have been studied in modern and future climates (36), paleoclimate evidence for such changes is limited; most studies have focused on ITCZ position (e.g., ref. 40). Our DA results suggest that ITCZ narrowing could be a defining characteristic of the PETM event. Relative to the model prior mean, the pre-PETM-DA posterior suggests a wider ITCZ, while the PETM posterior is more narrow (*SI Appendix*, Fig. S8). Proxies for relative moisture balance across the PETM are sparse, but comparison between the PETM-DA $P - E$ results and available data suggests generally good agreement, with clear evidence for increased rainfall in

the deep tropics and drying in the Gulf of Mexico and Tethys, consistent with a narrower ITCZ (Fig. 3A). The strong drying in the Gulf of Mexico in particular stands out as a notable result that emerges with the assimilation of the proxy data; in comparison, the model prior mean shows balanced $P - E$ in that region (*SI Appendix*, Fig. S8). Our DA results suggest that paleoclimate investigations of tropical and off-equatorial hydroclimatic changes are likely to shed light on how robust ITCZ narrowing is across ancient warm climates, with implications for future predictions.

In contrast with large changes in $P - E$ in the tropics, the annual changes in the hydrological cycle in the subtropics and midlatitudes (30 °N to 60 °N and 30 °S to 60 °S) are muted and regionally variable. At these latitudes, the PETM-DA suggests that seasonal changes in precipitation (i.e., those associated with monsoons or winter storm tracks) play a more important role. From December to March, winter storm tracks in the Pacific and Tethys Oceans are intensified, bringing heavy precipitation to northwestern North America and the proto-Mediterranean region; meanwhile, in the Southern Hemisphere, the South American monsoon intensified (Fig. 3E). From June to September, the African, Asian, and North American monsoon regions experienced elevated precipitation, while winter rainfall increased over southernmost South America and the Antarctic coastline (Fig. 3F). These results support midlatitude proxy evidence of a stronger seasonal cycle in precipitation with more severe, episodic events (11, 41). Although our model priors are too coarse to resolve features like atmospheric rivers (ARs), high-resolution (0.25°-atmosphere) PETM experiments with CESM show an increase in ARs in the Pacific and mid-Atlantic regions, in agreement with our inference of intensified winter storm tracks in these regions (42, 43).

Our model priors are isotope enabled; hence, we can also obtain posterior fields for the isotopes of precipitation, a useful point of comparison to water isotope proxies. The zonal mean annual response in precipitation δD (δD_P) shows systematic
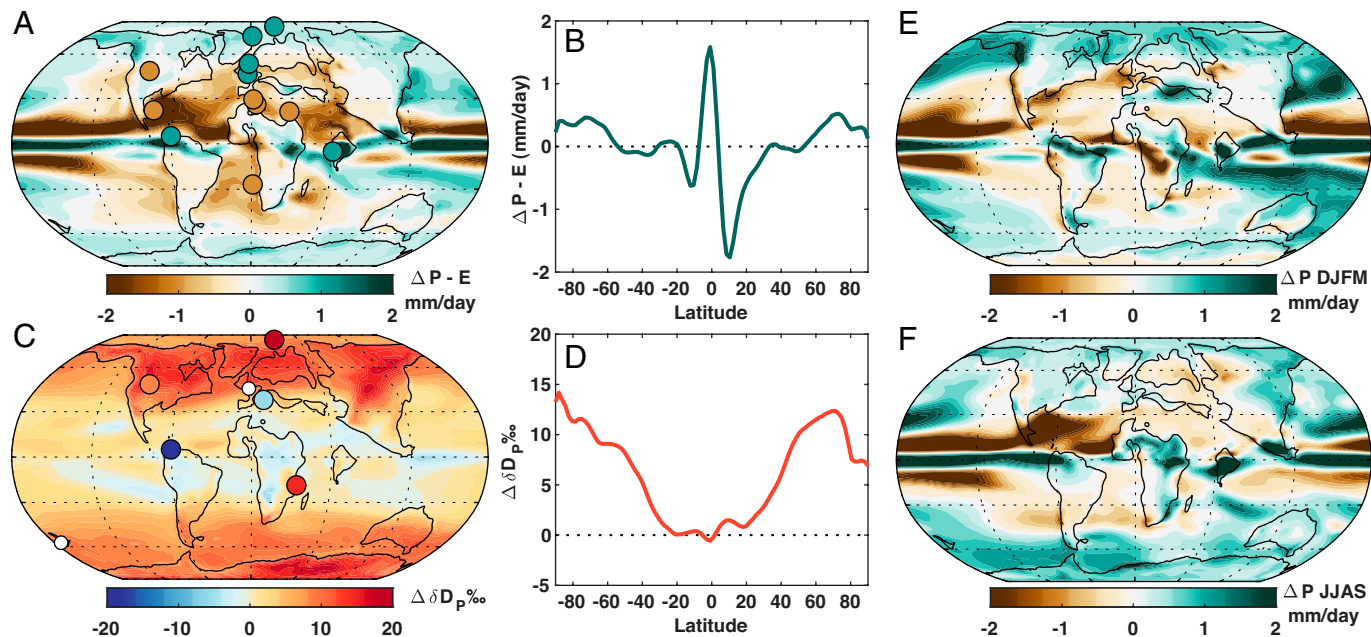

Fig. 3. Changes in the hydrological cycle during the PETM. All panels represent PETM − pre-PETM anomalies. (*A*) Change in mean annual precipitation minus evaporation ($P - E$) in the PETM-DA overlain with proxy indicators for relatively wetter (green) or drier (brown) conditions relative to the pre-PETM. Proxy data are from the compilation of ref. 12 with the addition of data from ref. 34 (*SI Appendix*). Proxy colors are qualitative and indicate the sign of change only. (*B*) Zonal mean annual change in $P - E$. (*C*) Change in the mean annual δD of precipitation (δD_P) in the PETM-DA overlain with inferred changes from leaf wax δD (Dataset S2). Sites with significant changes during the PETM are colored on the same scale as the DA results; sites without significant changes are plotted as smaller white dots. (*D*) Zonal mean annual change in δD_P. (*E*) The December to March (DJFM) change in precipitation (ΔP). (*F*) The June to September (JJAS) change in precipitation.

enrichment in the heavier isotope at the higher latitudes (Fig. 3*D*), with the most extreme change occurring over land (Fig. 3*C*). The latitudinal consistency of the isotopic response reflects the direct effect of warmer temperatures (and polar amplification) on isotopic fractionation as well as the fact that the warmer PETM atmosphere holds more water vapor, and thus, there is less Rayleigh distillation as vapor is exported to the polar regions (44). A similar response has been observed in high CO_2 simulations of the Cretaceous and the Eocene (44, 45).

The ∼20‰ increase that we observe in western North America and in the Arctic region agrees well with leaf wax reconstructions of δD_P from the Bighorn basin (46) and Lomonosov Ridge (10). Leaf wax data from the Tanzania and MAR2X (Venezuela) drill cores show a ca. 15‰ increase (47) and a 20‰ decrease (48), respectively; the PETM-DA reproduces the sign of change at these locations, although not the same magnitude (Fig. 3*C*). Leaf wax records from Vasterival (France) (49) and Kumara (New Zealand) (50) show no clear change across the PETM, while the PETM-DA suggests that an increase in δD_P should be registered at these sites (Fig. 3*C*). Several of the leaf wax sites, including Kumara and Tanzania, experienced a shift in organic matter source and/or an influx of fossil carbon during the PETM, which may affect the hydrogen isotopic composition (50, 51). More records of water isotope changes across the PETM are needed to fully validate the results from the PETM-DA, but it is encouraging that the reconstruction captures a large increase in high-latitude δD_P, a known feature of the event and of other warm climates as well (10, 44).

Climate Sensitivity. The PETM-DA yields an estimate of global temperature change that can be used to update our understanding of climate sensitivity during the PETM event and more broadly, investigate what equilibrium climate sensitivity (ECS) might be during an extremely warm climate.

In order to avoid having to account for the radiative impact of changes in paleogeography and solar luminosity (52), we calculate PETM ECS relative to the pre-PETM base climate rather than preindustrial conditions, following ref. 53. Given the absence of information about changes in trace greenhouse gases, we assume that CO_2 is the sole forcing agent. Although methane has long been suspected as a contributor to PETM warmth, any initial release of methane at the start of the event [i.e., from clathrate disassociation (54) or permafrost thaw (55)] would have been oxidized to CO_2 given the short residence time of methane in the atmosphere (ca. 9 y).

In this simple framework, the ECS calculation only requires constraints on the change in temperature and CO_2 (*SI Appendix*, Eqs. **3** and **4**). To obtain CO_2 constraints, we recalculate values from the two detailed planktic foraminiferal boron isotope ($\delta^{11}B$) records that span the PETM event (3, 56) using a Monte Carlo approach that accounts for uncertainties in seawater chemistry and physical properties (*SI Appendix*). Conversion of $\delta^{11}B$ pH estimates to CO_2 requires constraints on seawater temperature and one other parameter of the ocean carbonate system. For the former, we draw SST values for each core site from the posterior ensemble from the PETM-DA. For the latter, we sample across a wide range of plausible values for surface ocean saturation state (Ω; five to eight) to compute CO_2 and alkalinity (*Alk*) for the pre-PETM. We then increase *Alk* during the PETM by 300 μmol kg^{-1} following the carbonate chemistry solution from the PETM carbon-centric Grid Enabled Integrated Earth system model (cGENIE) simulation of ref. 3. (*SI Appendix*) and compute CO_2 for the PETM. We prefer this approach over drawing CO_2 directly from ref. 3. because

cGENIE-computed CO_2 is highly dependent on cGENIE SSTs and the static assumptions concerning the pre-PETM carbonate system. By using only the relative change in *Alk* from cGENIE (a conservative parameter), we minimize reliance on cGENIE model conditions, sample a wider range of initial ocean chemistry states, and leverage improved estimates of SST from the PETM-DA. We are also able to obtain narrower estimates for the change in CO_2 by calculating the pre-PETM and PETM states in a "paired" fashion (*SI Appendix*).

This calculation yields a pre-PETM CO_2 concentration of 1,120 ppm (850 to 1,460 ppm, 95% CI) and a PETM CO_2 concentration of 2,020 ppm (1,550 to 2,630 ppm, 95% CI) (*SI Appendix*, Table S1), resulting in 0.86 (0.76 to 0.97, 95% CI) CO_2 doublings (*SI Appendix*, Fig. S9) and a median ECS of 6.5 (5.7 to 7.4, 95% CI) (Fig. 4). This solution results in a drop in Ω of ca. 0.6 (*SI Appendix*, Table S1), in agreement with observations of ocean undersaturation (8, 58). However, it also assumes that weathering raises *Alk*, a reasonable assumption given that the body of the PETM spans ca. 70,000 y (59) and in agreement with carbon cycle modeling (3, 60, 61). We also explore end-member scenarios (i.e., holding either *Alk* or Ω constant across the PETM) to assess the sensitivity of the calculation to the carbonate system assumptions (*SI Appendix*).

Our ECS estimate for the PETM is higher than ref. 7 (3.6 °C) because this previous study used the cGENIE-computed CO_2 concentrations from ref. 3 (870 and 2,200 ppm for the pre-PETM and PETM, respectively). As noted, these values are highly dependent on cGENIE SSTs and its carbonate chemistry. Furthermore, while the estimates from ref. 3 lie within our uncertainty bounds for absolute CO_2, our paired calculation approach indicates that the 1.3 CO_2 doublings implied by these values are unlikely (*SI Appendix*, Fig. S9 and Table S1).

Given these revised $\delta^{11}B$-based estimates of the change in CO_2, it is unlikely that ECS during the PETM fell within the Intergovernmental Panel on Climate Change (IPCC) Sixth Assessment Report (AR6) 90% CI range of 2 °C to 5 °C (Fig. 4) (57). A PETM ECS of ca. 6 °C to 7 °C agrees with proxy-based estimates made for the Eocene (62, 63) and previous work, indicating that ECS may be much higher at elevated CO_2 concentrations due to low cloud feedbacks (6, 64, 65). Indeed, the Community Earth System Model 1.2 (CESM 1.2) has an ECS of 6.6 °C and 9.7 °C at three and six times preindustrial CO_2, respectively, under Eocene boundary conditions (note that our DA estimate for GMST is independent from CESM 1.2's ECS as the DA only compares proxy and model temperatures and is agnostic to the CO_2 concentration needed to generate said temperatures).
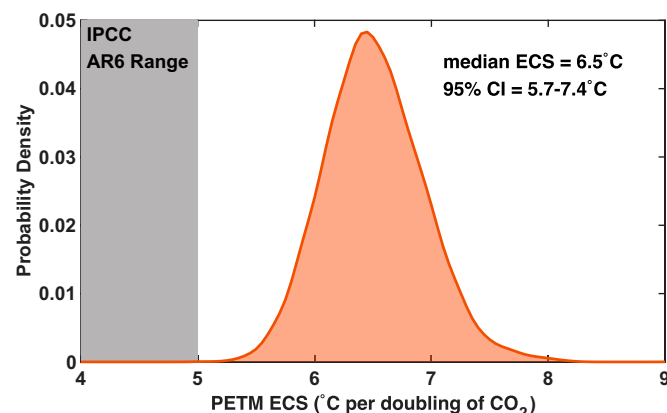
Fig. 4. Probability density function estimate of ECS during the PETM. Median and 95% values are given in the upper right. The 90% range of values reported in the IPCC AR6 Working Group I report is indicated by the gray bar (57).

However, our computed range of plausible ECS for the PETM is still broad (Fig. 4) because of the uncertainties and assumptions associated with estimating CO_2 and the limited amount of data available. More paleo-CO_2 studies are needed to further refine our estimate of ECS across the PETM.

Conclusions

The DA technique allows us to combine proxy estimates for temperature with fully coupled modeling experiments and produce a hybrid product that reveals spatial patterns of climate change during the PETM hyperthermal. Although the PETM proxy network is sparse (Fig. 1) and our ability to validate the PETM-DA is limited by the number of independent records available (Fig. 2D), the DA posterior yields a narrowed range of possible climate states and has features that agree with independent indicators for temperature and hydroclimate. The spatial patterns of temperature and $P - E$ changes during the PETM share similarities with future projections of climate change in response to anthropogenic emissions, including polar amplification (28), ITCZ narrowing (38), an intensification of monsoons (66), and stronger and more poleward-shifted winter storm tracks (67). Even though the PETM event was not as abrupt as human-caused climate change, features a different geographical distribution, and lacks some of the feedbacks that dominate warming patterns today (i.e., changes in the cryosphere), these broad similarities suggest that the large-scale response of the Earth system to a sudden emission of greenhouse gases is predictable and consistent even across millions of years of Earth history.

By leveraging the covariance structure of the climate model, the PETM-DA yields a more precise estimate of global warming during the PETM event that can be used to update our estimate of climate sensitivity. Using a Monte Carlo approach, we are able to narrow the estimation of CO_2 change over previous work. Our ECS estimate lies above the IPCC AR6 range, which suggests that PETM ECS is very likely higher than modern and near-future ECS. Since the pre-PETM climate lacks land ice and has limited sea ice, this high ECS is most likely associated with strong cloud feedbacks, as previous work has demonstrated (6, 64, 65). More high-resolution paleo-CO_2 studies are needed to refine PETM ECS further and also, to investigate whether elevated ECS is observed during other hyperthermal events in Earth history.

Materials and Methods

Extended methods are available in *SI Appendix*. Briefly, the data used in this reconstruction consist of four types of temperature proxies: the $\delta^{18}O$ of well-preserved (glassy) planktic foraminifera, the Mg/Ca of foraminifera, TEX$_{86}$, and the terrestrial MBT5$'_{Me}$ proxy. These data were drawn from the deepMIP compilation of ref. 14. as well as additional studies published more recently. The assimilation uses the average proxy value for each time slice. There are 35 and 33 proxy data points available for the PETM and pre-PETM slices, respectively, from 27 unique locations. The proxy data compilation is available in Dataset S1.

The climate model priors consist of 72 ensemble members from 14 new and preexisting simulations conducted with the fully coupled iCESM 1.2 (19, 20). Preexisting simulations include the Eocene simulations with three, six, and nine times preindustrial CO_2 (284.7 ppmv) that were described in refs. 6 and 68. These simulations used Early Eocene boundary conditions from deepMIP (18)

(*SI Appendix* has details) and were integrated for 2,000 y. For this study, we extended each of these simulations by 200 y using an updated formulation of the surface virtual salinity flux, which better resolves the seawater salinity in the Eocene Arctic Ocean. We also performed new iCESM 1.2 simulations to cover a wider range of atmospheric CO_2 (and surface temperatures) and Earth orbital configurations. Two simulations with 10 and 11 times preindustrial CO_2 were initialized from the 9 times simulation and run for 500 y. In addition, two suites of orbital sensitivity simulations were branched off of the three and six times simulations, representing minimum eccentricity and obliquity, high Northern Hemisphere seasonality, and high Southern Hemisphere seasonality (following the approach of ref. 69) (*SI Appendix* has details). The model priors have a wide range of GMST (24.6 °C to 41.7 °C) (Fig. 2B) due to the wide range of CO_2 concentrations used (854 to 3,132 ppm) and the nonlinear increase in climate sensitivity of the iCESM 1.2 model at high CO_2 concentrations (6).

The DA method is an offline ensemble square root Kalman filter approach following the methodology developed in refs. 21 and 22 using the MATLAB code package DASH (https://github.com/JonKing93/DASH). The posterior DA ensemble was internally validated using a leave-one-out method and then, externally assessed via comparison with independent terrestrial temperature proxies from the deepMIP compilation (14) (Fig. 2D).

For the calculation of climate sensitivity, we reassessed the change in atmospheric CO_2 during the PETM using boron isotopic data from marine core sites ODP 1209 (56) and Deep Sea Drilling Project (DSDP) 401 (3) and a Monte Carlo approach similar to ref. 70. We assumed a value for $\delta^{11}B_{sw}$ of 38.5‰ (± 0.2‰, 1σ) (71) and used the posterior of the PETM-DA to constrain temperature and salinity at the core site locations. The scenario shown in Fig. 4 samples Ω from five to eight during the pre-PETM and computes *Alk*, and then, it prescribes an increase in *Alk* of 300 µmol kg^{-1} during the PETM following the cGENIE simulation of ref. 3. Other scenarios and assumptions and a full explanation of the Monte Carlo approach are discussed in *SI Appendix*.

Data, Materials, and Software Availability. The posterior PETM-DA climate fields, proxy data used in the DA, and validation proxy data are available through Zenodo at https://doi.org/10.5281/zenodo.7096239 (72) and through GitHub at https://github.com/jesstierney/petmDA (Tierney 2022) (73). The DASH code is publicly available at https://github.com/JonKing93/DASH (74). The MATLAB code for the ECS calculations is available at https://github.com/St-Andrews-Isotope-Geochemistry/PETM_deltaCO2 (75).

Author affiliations: [a]Department of Geosciences, University of Arizona, Tucson, AZ 85721; [b]Climate and Global Dynamics Laboratory, National Center for Atmospheric Research, Boulder, CO 80305; [c]Key Laboratory of Orogenic Belts and Crustal Evolution, Ministry of Education, School of Earth and Space Sciences, Peking University, Beijing 100871, China; [d]Department of Earth and Planetary Sciences, University of California, Riverside, CA 92521; [e]Department of Atmospheric Sciences, University of Washington, Seattle, WA 98195; [f]Department of Earth and Environmental Sciences, University of Michigan, Ann Arbor, MI 48109; [g]School of Earth and Environmental Sciences, University of St. Andrews, St. Andrews KY16 9AL, United Kingdom; and [h]Department of Geosciences, Pennsylvania State University, University Park, PA 16802

1. F. A. McInerney, S. L. Wing, The Paleocene-Eocene Thermal Maximum: A perturbation of carbon cycle, climate, and biosphere with implications for the future. *Annu. Rev. Earth Planet. Sci.* **39**, 489–516 (2011).
2. S. K. Turner, Constraints on the onset duration of the Paleocene–Eocene Thermal Maximum. *Philos. Trans.- Royal Soc., Math. Phys. Eng. Sci.* **376**, 20170082 (2018).
3. M. Gutjahr *et al.*, Very large release of mostly volcanic carbon during the Palaeocene-Eocene Thermal Maximum. *Nature* **548**, 573–577 (2017).
4. L. L. Haynes, B. Hönisch, The seawater carbon inventory at the Paleocene-Eocene Thermal Maximum. *Proc. Natl. Acad. Sci. U.S.A.* **117**, 24088–24095 (2020).
5. T. D. Jones *et al.*, Climate model and proxy data constraints on ocean warming across the Paleocene–Eocene Thermal Maximum. *Earth Sci. Rev.* **125**, 123–145 (2013).
6. J. Zhu, C. J. Poulsen, J. E. Tierney, Simulation of Eocene extreme warmth and high climate sensitivity through cloud feedbacks. *Sci. Adv.* **5**, eaax1874 (2019).
7. G. N. Inglis *et al.*, Global mean surface temperature and climate sensitivity of the early Eocene Climatic Optimum (EECO), Paleocene–Eocene Thermal Maximum (PETM), and latest Paleocene. *Clim. Past* **16**, 1953–1968 (2020).
8. J. C. Zachos *et al.*, Rapid acidification of the ocean during the Paleocene-Eocene Thermal Maximum. *Science* **308**, 1611–1615 (2005).

9. W. Yao, A. Paytan, U. G. Wortmann, Large-scale ocean deoxygenation during the Paleocene-Eocene Thermal Maximum. *Science* **361**, 804–806 (2018).
10. M. Pagani *et al.*; Expedition 302 Scientists, Arctic hydrology during global warming at the Palaeocene/Eocene Thermal Maximum. *Nature* **442**, 671–675 (2006).
11. B. Schmitz, V. Pujalte, Abrupt increase in seasonal extreme precipitation at the Paleocene-Eocene boundary. *Geology* **35**, 215–218 (2007).
12. M. J. Carmichael *et al.*, Hydrological and associated biogeochemical consequences of rapid global warming during the Paleocene-Eocene Thermal Maximum. *Global Planet. Change* **157**, 114–138 (2017).
13. J. E. Tierney *et al.*, Past climates inform our future. *Science* **370**, eaay3701 (2020).
14. C. J. Hollis *et al.*, The DeepMIP contribution to PMIP4: Methodologies for selection, compilation and analysis of latest Paleocene and early Eocene climate proxy data, incorporating version 0.1 of the DeepMIP database. *Geosci. Model Dev.* **12**, 3149–3206 (2019).
15. J. Frieling *et al.*, Extreme warmth and heat-stressed plankton in the tropics during the Paleocene-Eocene Thermal Maximum. *Sci. Adv.* **3**, e1600891 (2017).
16. D. J. Lunt *et al.*, DeepMIP: Model intercomparison of early Eocene climatic optimum (EECO) large-scale climate features and comparison with proxy data. *Clim. Past* **17**, 203–227 (2021).
17. N. Herold *et al.*, A suite of early Eocene (∼55 Ma) climate model boundary conditions. *Geosci. Model Dev.* **7**, 2077–2090 (2014).
18. D. J. Lunt *et al.*, The DeepMIP contribution to PMIP4: Experimental design for model simulations of the EECO, PETM, and pre-PETM (version 1.0). *Geosci. Model Dev.* **10**, 889–901 (2017).
19. J. W. Hurrell *et al.*, The community Earth system model: A framework for collaborative research. *Bull. Am. Meteorol. Soc.* **94**, 1339–1360 (2013).
20. E. Brady *et al.*, The connected isotopic water cycle in the Community Earth System Model version 1. *J. Adv. Model. Earth Syst.* **11**, 2547–2566 (2019).
21. J. E. Tierney *et al.*, Glacial cooling and climate sensitivity revisited. *Nature* **584**, 569–573 (2020).
22. M. B. Osman *et al.*, Globally resolved surface temperatures since the Last Glacial Maximum. *Nature* **599**, 239–244 (2021).
23. H. J. Spero, J. Bijma, D. W. Lea, B. E. Bemis, Effect of seawater carbonate concentration on foraminiferal carbon and oxygen isotopes. *Nature* **390**, 497–500 (1997).
24. R. E. Zeebe, An explanation of the effect of seawater carbonate concentration on foraminiferal oxygen isotopes. *Geochim. Cosmochim. Acta* **63**, 2001–2007 (1999).
25. R. Zeebe, An expression for the overall oxygen isotope fractionation between the sum of dissolved inorganic carbon and water. *Geochem. Geophys. Geosystems* **8**, Q09002 (2007).
26. J. Uchikawa, R. E. Zeebe, Examining possible effects of seawater pH decline on foraminiferal stable isotopes during the Paleocene-Eocene Thermal Maximum. *Paleoceanography* **25**, PA2216 (2010).
27. D. J. Lunt *et al.*, On the causes of mid-Pliocene warmth and polar amplification. *Earth Planet. Sci. Lett.* **321**, 128–138 (2012).
28. L. C. Hahn, K. C. Armour, M. D. Zelinka, C. M. Bitz, A. Donohoe, Contributions to polar amplification in CMIP5 and CMIP6 models. *Front. Earth Sci* **9**, 710036 (2021).
29. C. Robert, J. P. Kennett, Antarctic subtropical humid episode at the Paleocene-Eocene boundary: Clay-mineral evidence. *Geology* **22**, 211–214 (1994).
30. R. DeConto, D. Pollard, D. Harwood, Sea ice feedback and Cenozoic evolution of Antarctic climate and ice sheets. *Paleoceanography* **22**, PA3214 (2007).
31. K. E. Snell *et al.*, Hot summers in the Bighorn Basin during the early Paleogene. *Geology* **41**, 55–58 (2013).
32. G. Suan *et al.*, Subtropical climate conditions and mangrove growth in Arctic Siberia during the early Eocene. *Geology* **45**, 539–542 (2017).
33. D. A. Willard *et al.*, Arctic vegetation, temperature, and hydrology during Early Eocene transient global warming events. *Global Planet. Change* **178**, 139–152 (2019).
34. V. Smith *et al.*, Life and death in the Chicxulub impact crater: A record of the Paleocene–Eocene Thermal Maximum. *Clim. Past* **16**, 1889–1899 (2020).
35. K. Wodzicki, A. Rapp, Long-term characterization of the Pacific ITCZ using TRMM, GPCP, and ERA-Interim. *J. Geophys. Res. Atmos.* **121**, 3153–3170 (2016).
36. M. P. Byrne, A. G. Pendergrass, A. D. Rapp, K. R. Wodzicki, Response of the intertropical convergence zone to climate change: Location, width, and strength. *Curr. Clim. Change Rep.* **4**, 355–370 (2018).
37. W. K. Lau, K. M. Kim, Robust Hadley Circulation changes and increasing global dryness due to CO2 warming from CMIP5 model projections. *Proc. Natl. Acad. Sci. U.S.A.* **112**, 3630–3635 (2015).
38. M. P. Byrne, T. Schneider, Narrowing of the ITCZ in a warming climate: Physical mechanisms. *Geophys. Res. Lett.* **43**, 11–350 (2016).
39. J. Neelin, C. Chou, H. Su, Tropical drought regions in global warming and El Niño teleconnections. *Geophys. Res. Lett.* **30**, 2275 (2003).
40. D. McGee, A. Donohoe, J. Marshall, D. Ferreira, Changes in ITCZ location and cross-equatorial heat transport at the Last Glacial Maximum, Heinrich Stadial 1, and the mid-Holocene. *Earth Planet. Sci. Lett.* **390**, 69–79 (2014).
41. B. Z. Foreman, P. L. Heller, M. T. Clementz, Fluvial response to abrupt global warming at the Palaeocene/Eocene boundary. *Nature* **491**, 92–95 (2012).
42. C. A. Shields, J. T. Kiehl, W. Rush, M. Rothstein, M. A. Snyder, Atmospheric rivers in high-resolution simulations of the Paleocene Eocene Thermal Maximum (PETM). *Palaeogeogr. Palaeoclimatol. Palaeoecol.* **567**, 110293 (2021).
43. W. D. Rush, J. T. Kiehl, C. A. Shields, J. C. Zachos, Increased frequency of extreme precipitation events in the North Atlantic during the PETM: Observations and theory. *Palaeogeogr. Palaeoclimatol. Palaeoecol.* **568**, 110289 (2021).

44. E. N. Speelman *et al.*, Modeling the influence of a reduced equator-to-pole sea surface temperature gradient on the distribution of water isotopes in the Early/Middle Eocene. *Earth Planet. Sci. Lett.* **298**, 57–65 (2010).
45. C. J. Poulsen, D. Pollard, T. S. White, General circulation model simulation of the δ18O content of continental precipitation in the middle Cretaceous: A model-proxy comparison. *Geology* **35**, 199–202 (2007).
46. F. A. Smith, S. L. Wing, K. H. Freeman, Magnitude of the carbon isotope excursion at the Paleocene–Eocene Thermal Maximum: The role of plant community change. *Earth Planet. Sci. Lett.* **262**, 50–65 (2007).
47. L. Handley, P. N. Pearson, I. K. McMillan, R. D. Pancost, Large terrestrial and marine carbon and hydrogen isotope excursions in a new Paleocene/Eocene boundary section from Tanzania. *Earth Planet. Sci. Lett.* **275**, 17–25 (2008).
48. C. Jaramillo *et al.*, Effects of rapid global warming at the Paleocene-Eocene boundary on neotropical vegetation. *Science* **330**, 957–961 (2010).
49. S. Garel *et al.*, Paleohydrological and paleoenvironmental changes recorded in terrestrial sediments of the Paleocene–Eocene boundary (Normandy, France). *Palaeogeogr. Palaeoclimatol. Palaeoecol.* **376**, 184–199 (2013).
50. L. Handley, E. M. Crouch, R. D. Pancost, A New Zealand record of sea level rise and environmental change during the Paleocene–Eocene Thermal Maximum. *Palaeogeogr. Palaeoclimatol. Palaeoecol.* **305**, 185–200 (2011).
51. S. L. Lyons *et al.*, Palaeocene–Eocene Thermal Maximum prolonged by fossil carbon oxidation. *Nat. Geosci.* **12**, 54–60 (2019).
52. A. Farnsworth *et al.*, Climate sensitivity on geological timescales controlled by nonlinear feedbacks and ocean circulation. *Geophys. Res. Lett.* **46**, 9880–9889 (2019).
53. G. Shaffer, M. Huber, R. Rondanelli, J. O. Pepke Pedersen, Deep time evidence for climate sensitivity increase with warming. *Geophys. Res. Lett.* **43**, 6538–6545 (2016).
54. G. R. Dickens, M. M. Castillo, J. C. Walker, A blast of gas in the latest Paleocene: Simulating first-order effects of massive dissociation of oceanic methane hydrate. *Geology* **25**, 259–262 (1997).
55. R. M. DeConto *et al.*, Past extreme warming events linked to massive carbon release from thawing permafrost. *Nature* **484**, 87–91 (2012).
56. D. E. Penman, B. Hönisch, R. E. Zeebe, E. Thomas, J. C. Zachos, Rapid and sustained surface ocean acidification during the Paleocene-Eocene Thermal Maximum. *Paleoceanography* **29**, 357–369 (2014).
57. P. Forster *et al.*, "The Earth's energy budget, climate feedbacks, and climate sensitivity" in *Climate Change 2021: The Physical Science Basis. Working Group I Contribution to the Sixth Assessment Report of the Intergovernmental Panel on Climate Change*, V. Masson-Delmotte *et al.*, Eds. (Cambridge University Press, Cambridge, United Kingdom, 2021), pp. 923–1054.
58. T. J. Bralower *et al.*, Evidence for shelf acidification during the onset of the Paleocene-Eocene Thermal Maximum. *Paleoceanogr. Paleoclimatol.* **33**, 1408–1426 (2018).
59. U. Röhl, T. Westerhold, T. J. Bralower, J. C. Zachos, On the duration of the Paleocene-Eocene Thermal Maximum (PETM). *Geochem. Geophys. Geosystems* **8**, Q12002 (2007).
60. A. Ridgwell, D. N. Schmidt, Past constraints on the vulnerability of marine calcifiers to massive carbon dioxide release. *Nat. Geosci.* **3**, 196–200 (2010).
61. Y. Cui *et al.*, Slow release of fossil carbon during the Palaeocene–Eocene Thermal Maximum. *Nat. Geosci.* **4**, 481–485 (2011).
62. M. J. Cramwinckel *et al.*, Synchronous tropical and polar temperature evolution in the Eocene. *Nature* **559**, 382–386 (2018).
63. E. Anagnostou *et al.*, Proxy evidence for state-dependence of climate sensitivity in the Eocene greenhouse. *Nat. Commun.* **11**, 4436 (2020).
64. R. Caballero, M. Huber, State-dependent climate sensitivity in past warm climates and its implications for future climate projections. *Proc. Natl. Acad. Sci. U.S.A.* **110**, 14162–14167 (2013).
65. T. Schneider, C. M. Kaul, K. G. Pressel, Possible climate transitions from breakup of stratocumulus decks under greenhouse warming. *Nat. Geosci.* **12**, 163–167 (2019).
66. B. Wang, C. Jin, J. Liu, Understanding future change of global monsoons projected by CMIP6 models. *J. Clim.* **33**, 6471–6489 (2020).
67. T. A. Shaw, Mechanisms of future predicted changes in the zonal mean mid-latitude circulation. *Curr. Clim. Change Rep.* **5**, 345–357 (2019).
68. J. Zhu *et al.*, Simulation of early Eocene water isotopes using an Earth system model and its implication for past climate reconstruction. *Earth Planet. Sci. Lett.* **537**, 116164 (2020).
69. D. J. Lunt *et al.*, A model for orbital pacing of methane hydrate destabilization during the Palaeogene. *Nat. Geosci.* **4**, 775–778 (2011).
70. J. W. Rae *et al.*, Atmospheric CO2 over the past 66 million years from marine archives. *Annu. Rev. Earth Planet. Sci.* **49**, 609–641 (2021).
71. E. Anagnostou *et al.*, Changing atmospheric CO2 concentration was the primary driver of early Cenozoic climate. *Nature* **533**, 380–384 (2016).
72. J. Tierney, jesstierney/petmDA: petmDA v1.0. Zenodo. https://zenodo.org/record/7096239. Deposited 20 September 2022.
73. J. Tierney, petmDA. GitHub. https://github.com/jesstierney/petmDA. Deposited 26 March 2022.
74. J. King, JonKing93/DASH. GitHub. https://github.com/JonKing93/DASH. Deposited 11 March 2020.
75. J. Tierney, St-Andrews-Isotope-Geochemistry/PETM_deltaCO2. GitHub. https://github.com/St-Andrews-Isotope-Geochemistry/PETM_deltaCO2. Deposited 26 March 2022.